Journal of Alloys and Compounds 844 (2020) 156147

Contents lists available at ScienceDirect

Journal of Alloys and Compounds

journal homepage: http://www.elsevier.com/locate/jalcom

Boosted photocatalytic Cr(VI) reduction over Z-scheme MIL-53(Fe)/$Bi_{12}O_{17}Cl_2$ composites under white light

Hua Li [a], Chen Zhao [a, b], Xia Li [a], Huifen Fu [b], Zhihua Wang [a, **], Chong-Chen Wang [b, *]

[a] State Key Laboratory of Chemical Resource Engineering, Beijing University of Chemical Technology, Beijing, 100029, China
[b] Beijing Key Laboratory of Functional Materials for Building Structure and Environment Remediation/Beijing Advanced Innovation Centre for Future Urban Design, Beijing University of Civil Engineering and Architecture, Beijing, 100044, China

ARTICLE INFO

Article history:
Received 27 March 2020
Received in revised form
7 June 2020
Accepted 19 June 2020
Available online 25 June 2020

Keywords:
MIL-53(Fe)
$Bi_{12}O_{17}Cl_2$ nanosheet
Composite
Cr(VI) reduction
White light

ABSTRACT

Series MIL-53(Fe)/$Bi_{12}O_{17}Cl_2$ (MB*x*) composites were constructed via facile ball-milling treatment of the MIL-53(Fe) octahedrons and $Bi_{12}O_{17}Cl_2$ nanosheets. The addition of a specific quality of $Bi_{12}O_{17}Cl_2$ was in favor of strengthening the transfer ability of photo-generated charge carriers in the composites, thereby further enhancing the photocatalytic performance. Being compared with pristine MIL-53(Fe) and $Bi_{12}O_{17}Cl_2$, the MB*x* composites exhibited superior white-light-driven Cr(VI) photoreduction performance. The optimal MB100 photocatalyst displayed the best photocatalytic activity, in which 99.2% Cr(VI) can be eliminated within 90 min under white light illumination. Under the identical reaction conditions, it achieved 42.9% and 76.5% higher improvements as those of pure MIL-53(Fe) and $Bi_{12}O_{17}Cl_2$. More than that, the MB100 also demonstrated good stability even after four cycles of testing experiments. At last, the corresponding reaction mechanism was clarified based on the electrochemical analysis and electron spin resonance (ESR) data. Such heterogeneous photocatalyst design strategy based on Fe-MOFs and bismuth-rich bismuth oxyhalides might provide new insights for treating Cr-containing wastewater.

1. Introduction

Environmental contamination is a serious problem threatening the sustainable development of human society. The common pollutants include heavy metals (HMs) [1], persistent organic pollutants (POPs) [2,3], pharmaceutical and personal care products (PPCPs) [4], organic dyes [5], etc. Among them, Cr is a typical HMs, which is commonly produced by leather tanning, textile manufacturing, steel manufacturing, printing, pigment and other industries [6,7]. Cr has two main valence states, in which Cr(VI) is a highly carcinogenic, mutation-causing toxic substance, whereas Cr(III) is an important substance to regulate sugar metabolism for humans. As a consequence, the transformation of Cr(VI) to Cr(III) has attracted increasing attentions. The conventional treatment techniques include ion exchange [8], membrane separation [9], ion exchange [9], electrolysis [10], chemical precipitation [11]. The photocatalytic reduction method has received much attention due to its prominent advantages, such as mild reaction condition, minimal secondary pollution, high-level efficiency and reutilization properties [12–15].

BiOX (X = Cl, Br, I) materials have induced a huge amount of interest owing to their good chemical stability, characteristic energy band structures and multitudinous morphologies [16–20]. However, it should be admitted that BiOX-based photocatalysts are still unsatisfactory for actual applications owing to the limited absorption capacity for real sunlight and low photo-generated hole-electron pairs separation efficiency [21]. Recently, density functional theory calculation (DFT) indicates that the preparation of bismuth halide with different atomic ratios might be inclined to yield amounts of novel photocatalysts with different energy band structures [22–26]. For example, the high yield $Bi_{12}O_{17}Cl_2$ nanosheet was synthesized via solvothermal method to regulate the atomic ratio of O and Cl [27]. Considering the band gap of $Bi_{12}O_{17}Cl_2$ is narrow (approximately 2.07 eV) [27], thus making it possess ability to utilize sunlight light more effectively. Furthermore, as the conduction band position of $Bi_{12}O_{17}Cl_2$ is negative enough, so the molecular oxygen (O_2) could transform into hydroxyl radicals (·OH) through two-electron reaction process, which has proved to be extremely significant for degradation of organic contaminants [27].

* Corresponding author.
** Corresponding author.
E-mail addresses: zhwang@mail.buct.edu.cn (Z. Wang), wangchongchen@bucea.edu.cn, chongchenwang@126.com (C.-C. Wang).

https://doi.org/10.1016/j.jallcom.2020.156147
0925-8388/

Nevertheless, the pure $Bi_{12}O_{17}Cl_2$ photocatalyst was limited by its relatively low utilization efficiency of photo-generated carriers, so many researchers attempted to construct $Bi_{12}O_{17}Cl_2$-based composites to further improve their photocatalytic activities, such as $Bi_{12}O_{17}Cl_2$/β-Bi_2O_3 [22], AgI/$Bi_{12}O_{17}Cl_2$ [23], BiOI/$Bi_{12}O_{17}Cl_2$ [25].

Metal organic frameworks (MOFs) is a variety of three-dimensional porous crystalline materials constructed by self-assembly process of organic linkers and metal ions [28,29]. MOFs are beginning to appear in a wide range of applications, like catalysis [30–33], gas adsorption/storage [34], molecular separation [35] and chemical sensing [36]. MIL-53(Fe) recently has attracted much scientific interest due to its special properties, which is synthesized from Fe(III) ions and terephthalic acid with a band gap of 2.82 eV [37]. It possesses prominent chemical and thermal robustness capabilities, thus make it a distinguished photocatalyst for various redox reactions. However, with respect to pristine materials, the photocatalytic efficiency of MIL-53(Fe) is low owing to its poor electric conductivity [21]. Therefore, its photocatalytic performance can be further improved by forming heterojunction structure with other semiconductors. For example, Tang et al. [38] prepared MIL-53(Fe)/BiOBr composites by co-precipitation strategy, which possessed good photodegradation capacity for rhodamine B (RhB) and carbamazepine under visible light illumination. Huang et al. [39] prepared MIL-53(Fe)/C_3N_4 composites through solvothermal method, the optimal photocatalyst achieved 100.0% of Cr(VI) reduction efficiency within 180 min upon illumination under visible light. Hu et al. [40] constructed CdS/MIL-53(Fe) composites to photodegradation of RhB, which showed reinforced photocatalytic performance compared to pure component. But so far, there are no reports about heterogeneous photocatalyst prepared through MIL-53(Fe) and $Bi_{12}O_{17}Cl_2$ nanosheet.

Based on the above considerations, we prepared MIL-53(Fe)/$Bi_{12}O_{17}Cl_2$ (MB*x*) composites via facile and controllable ball-milling method. Their physicochemical and electrooptical properties were explored by many kinds of characterization techniques. The photoreduction of Cr(VI) was conducted over the as-prepared photocatalysts, and the experimental results suggested that the formation of composites between MIL-53(Fe) and $Bi_{12}O_{17}Cl_2$ could enhance the transfer efficiency of photo-generated charge carriers compared with the pristine component. In addition, the rational reaction mechanism was proposed on the account of the experimental consequences.

2. Experimental

2.1. Materials preparation

2.1.1. Fabrication of MIL-53(Fe) and $Bi_{12}O_{17}Cl_2$ photocatalysts

Both the MIL-53(Fe) and $Bi_{12}O_{17}Cl_2$ were prepared by solvothermal methods according to the previous studies [21,27,38,41]. The details of the synthesis procedures were illustrated in the Electronical Supporting Information.

Table 1
The preparations of the MB*x* composites with various dosages of $Bi_{12}O_{17}Cl_2$.

No.	MIL-53(Fe) (mg)	$Bi_{12}O_{17}Cl_2$ (mg)	Material
1	100	50	MB50
2	100	100	MB100
3	100	200	MB200
4	100	300	MB300

2.1.2. Fabrication of MB*x* composites

MIL-53(Fe)/$Bi_{12}O_{17}Cl_2$ composites were constructed by facile ball-milling method. As shown in Table 1, 100.0 mg MIL-53(Fe) and various amount of $Bi_{12}O_{17}Cl_2$ were evenly added in a planetary ball-milling instrument and ran at 30 Hz for 20 min. The products were represented as MB*x*, namely MB50, MB100, MB200 and MB300. A brief schematic illustration of photocatalysis procedure was depicted in Fig. 1.

2.2. Photocatalytic efficiency evaluation

The photoreduction performances of different photocatalysts were assessed by the conversion efficiencies from Cr(VI) to Cr(III). More specifically, the addition of the photocatalyst in the reactor was guaranteed to be 0.5 g/L and the initial concentration of Cr(VI) was determined to 10 mg/L. Meanwhile, the pH values of the solutions were regulated by 0.1 M H_2SO_4 or 0.2 M NaOH solution. After 30 min of adsorption-desorption equilibrium under dark condition, the subsequent experiments were carried out under xenon light illumination. Next, 2.0 mL solution was extracted and filtered through 0.45 μm filter membranes at pre-set time for follow-up tests. The Cr(VI) content in the filtrate was tested by 1,5-diphenyl carbonyl dihydrazine colorimetry at the maximum absorption wavelength of 540 nm using a double-beam ultraviolet spectrophotometer (UV–vis, Persee, TU-1901).

Meanwhile, the details about the different types of characterization techniques (PXRD, FTIR, SEM, TEM, HRTEM, XPS, UV–vis DRS, FL and ESR) and the electrochemical analysis were illustrated in Electronic Supplementary Material.

3. Results and discussions

3.1. Characterizations

Fig. 2(a) showed the PXRD patterns of $Bi_{12}O_{17}Cl_2$, MIL-53(Fe), and MB*x* composites. The characteristic peaks of the synthesized $Bi_{12}O_{17}Cl_2$ were in good accordance with a tetragonal phase (No.37–0702), in which the obvious diffraction peaks located at 26.4°, 29.2°, 30.4°, 32.9° and 47.2° indexed to the (1 1 5), (1 1 7), (0 0 12), (2 0 0) and (2 2 0) crystal planes, respectively. Furthermore, there were no undefined diffraction peaks in the PXRD pattern of $Bi_{12}O_{17}Cl_2$, suggesting that $Bi_{12}O_{17}Cl_2$ was successfully synthesized. Additionally, MIL-53(Fe) matched well with the characteristic diffraction peaks reported in previous study [42]. In the PXRD spectra of MB*x* composites, the principal peaks of $Bi_{12}O_{17}Cl_2$ can be clearly detected, but the diffraction peaks of pristine MIL-53(Fe) were particularly weak. This phenomenon can be ascribed to the peak intensities of $Bi_{12}O_{17}Cl_2$ were relatively greater than that of MIL-53(Fe), which was similar to the reported studies about MOFs/Bi-based composites [43,44].

The FTIR spectra of as-obtained materials were illustrated in Fig. 2(b). As for MIL-53(Fe), the strong peaks at 1500 cm^{-1} and 1384 cm^{-1} were attributed to the symmetric and asymmetric vibration of C=O bonds, respectively [45]. Importantly, the vibration peak at 747 cm^{-1} corresponded to C–H bond of benzene rings originated from the dicarboxylate ligands in MIL-53(Fe) [46,47]. In addition, the characteristic peak at 538 cm^{-1} indicated the presence of metal-oxygen bonding between 1,4-BDC and Fe(III) [48]. Furthermore, all MB*x* composites displayed characteristic peaks around 3418 cm^{-1} and 512 cm^{-1}, which were attributed to –OH bending vibration of H_2O molecules and the Bi–O stretching vibrations in $Bi_{12}O_{17}Cl_2$, respectively [49,50]. Combing PXRD and FTIR analysis, it could be considered that the successful formation of MB*x* composites via ball-milling method.

Fig. 3 exhibited the morphologies of MIL-53(Fe), $Bi_{12}O_{17}Cl_2$ and

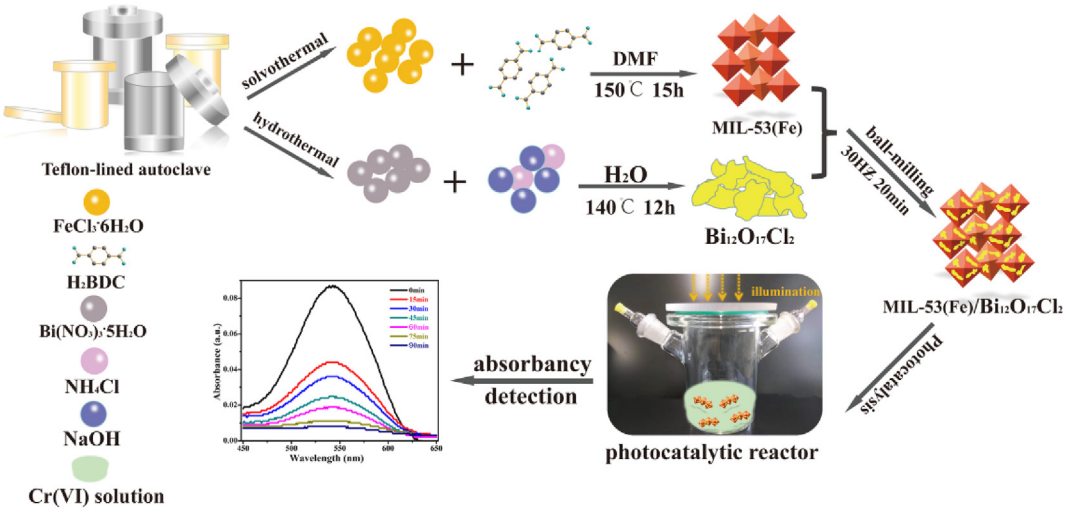

Fig. 1. A brief schematic diagram of the experimental process.

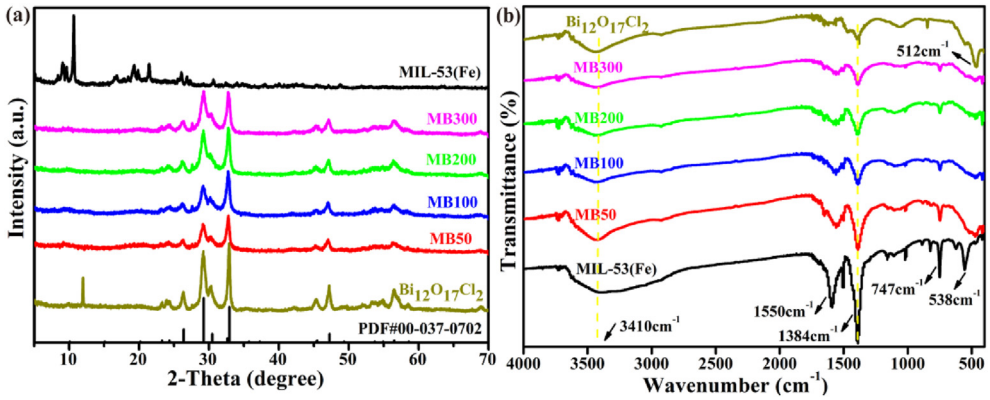

Fig. 2. (a) PXRD patterns and (b) FTIR spectra of MIL-53(Fe), $Bi_{12}O_{17}Cl_2$ and MB*x* composites.

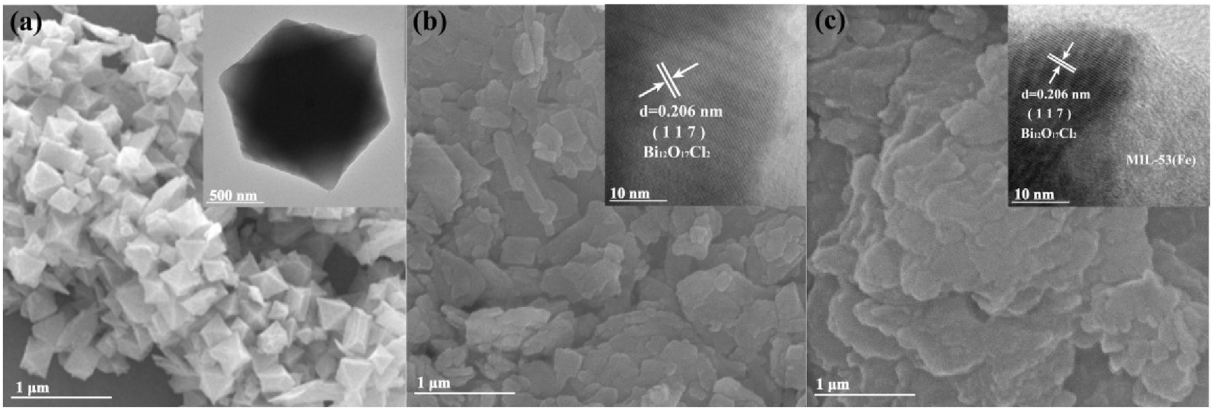

Fig. 3. SEM and HRTEM micrographs of (a) MIL-53(Fe), (b) $Bi_{12}O_{17}Cl_2$ and (c) MB100.

MB100. MIL-53(Fe) crystals displayed regular octahedrons morphology with glossy surface, and the particle size were hundreds of nanometers (Fig. 3(a)), which was accordance with previous studies [21]. The SEM and HRTEM micrographs (Fig. 3(b)) showed that the $Bi_{12}O_{17}Cl_2$ displayed the irregular nanosheet structure, which possessed an uneven size of 100–500 nm in length and 100–200 nm in width. The SEM micrograph of BM100 (Fig. 3(c)) suggested that $Bi_{12}O_{17}Cl_2$ with different shapes were covered on the surface of MIL-53(Fe) after ball-milling process. The corresponding HRTEM image (Fig. 3(c)) further indicated that the MB*x* composites can be successfully formed between $Bi_{12}O_{17}Cl_2$ (black parts) and MIL-53(Fe) (grey parts). Additionally, the HRTEM image of MB100 showed the fringe spacing of 0.206 nm, being assigned to the (1 1 7) crystal plane of $Bi_{12}O_{17}Cl_2$ (JCPDS

No.37−0702). The above results indicated that $Bi_{12}O_{17}Cl_2$ was successfully combined with MIL-53(Fe).

The binding states of the MB100 were detected by XPS instrument. The survey spectrum proved that C, O, Cl, Fe and Bi elements were present in the MB100 (Fig. 4(a)). The C 1s spectrum (Fig. 4(b)) ought to be divided into two peaks of 284.9, and 288.8 eV, which corresponded to the C−C bond of the benzene ring and C═O bond presented in terephthalic acid, respectively [51]. The O 1s XPS spectrum (Fig. 4(c)) should be curve-fitted into two peaks at 530.7 and 531.8 eV, respectively, which were ascribed to the Fe−O/Bi−O and C═O functional groups [52]. The Cl 2p spectrum in Fig. 4(d) was split up two binding energy peaks at 198.4 and 200.0 eV, respectively, which was contributed to Cl $2p_{3/2}$ and Cl $2p_{1/2}$ [53]. The Fe 2p spectrum in Fig. 4(e) indicated that the two peaks located at 712.2 and 725.6 eV, which were indexed to Fe $2p_{3/2}$ and Fe $2p_{1/2}$, respectively [54]. Additionally, there was the other peak at 718.4 eV, which was the satellite signal peak and proved the existence of Fe(III) species in the MB100 [55,56]. Moreover, the characteristic peaks at 159.6 eV and 164.9 eV in Bi 4f spectrum (Fig. 4(f)) were correlated with Bi $4f_{7/2}$ and Bi $4f_{5/2}$, respectively [57]. After compounding MIL-53(Fe) and $Bi_{12}O_{17}Cl_2$ through ball-milling process, the peaks in Bi 4f spectra of different MB*x* composites shifted towards lower binding energies compared with pristine $Bi_{12}O_{17}Cl_2$, confirming the existence of electron transfer from $Bi_{12}O_{17}Cl_2$ to MIL-53(Fe) [58,59].

The UV−vis DRS spectra of the different photocatalysts were demonstrated in Fig. 5(a). The results suggested that the maxima absorption edge of MIL-53(Fe) was at approximately 438 nm, and the $Bi_{12}O_{17}Cl_2$ exhibited visible light absorption at wavelength about 599 nm. Additionally, with the increase dosages of $Bi_{12}O_{17}Cl_2$, the absorption edge curves were gradually similar with that of pure $Bi_{12}O_{17}Cl_2$. However, it was worth noting that all the as-prepared MB*x* composites possessed absorption ability both in ultraviolet and visible regions, revealing that they can be deemed as UV−visible-light-responsive photocatalysts.

The corresponding band gap energy (E_g) values were calculated following Eq. (1) [60].

$$Ah\upsilon = k(h\upsilon - Eg)^{n/2} \quad (1)$$

where *A*, *h*, *ν*, and *k* represent the absorption coefficient, Planck's constant, the light frequency and a constant, respectively, *n* is rested with the optical transition type of the photocatalyst. According to the previous literatures, MIL-53(Fe) should be regarded as indirect semiconductor ($n = 4$) [61,62], whereas $Bi_{12}O_{17}Cl_2$ can be deemed as direct semiconductor ($n = 1$) [27]. From the Tauc plots in Fig. 5(b), the E_g values of MIL-53(Fe) and $Bi_{12}O_{17}Cl_2$ were about 2.83 eV and 2.08 eV, respectively, which were close to the previous literatures [38−42]. Furthermore, the E_g values of MB50, MB100, MB200 and MB300 were estimated to be 2.59 eV, 2.68 eV, 2.73 eV and 2.74 eV, respectively.

3.2. Cr(VI) removal

The Cr(VI) photoreduction efficiencies over $Bi_{12}O_{17}Cl_2$, MIL-53(Fe) and MB*x* composites were assessed under white light illumination, as displayed in Fig. 6(a). It was obvious that Cr(VI) concentration hardly changed in the absence of MB100 after 120 min illumination time. Furthermore, under the same experimental circumstance, all the MB*x* composites exhibited better photoreduction activities than that of pristine MIL-53(Fe) (68.2%) and $Bi_{12}O_{17}Cl_2$ (23.3%) photocatalysts. Additionally, the MB100 displayed more effective white-light-responsive photocatalytic performance for reducing Cr(VI), namely 99.2% of Cr(VI) ions can be completely removed within 90 min. This result should be ascribed to the excellent photo-generated carriers transfer at the MIL-53(Fe)/$Bi_{12}O_{17}Cl_2$ interface. Moreover, the pseudo-first-order dynamic model ($\ln[C_0/C_t] = kt$) was used to calculate the photocatalytic rates over various photocatalysts. As shown in Fig. 6(b), the order of *k* values was as follows: MB100 (0.0284 min^{-1}) > MB50 (0.0246 min^{-1}) > MB200 (0.0239 min^{-1}) > MB300 (0.0146 min^{-1}) > MIL-53(Fe) (0.0041 min^{-1}) > $Bi_{12}O_{17}Cl_2$ (0.0025 min^{-1}). Meanwhile, the comparison of photocatalytic efficiency between MB100 and the other categories of photocatalysts were listed in Table S1 in the Electronical Supporting Information, suggesting that

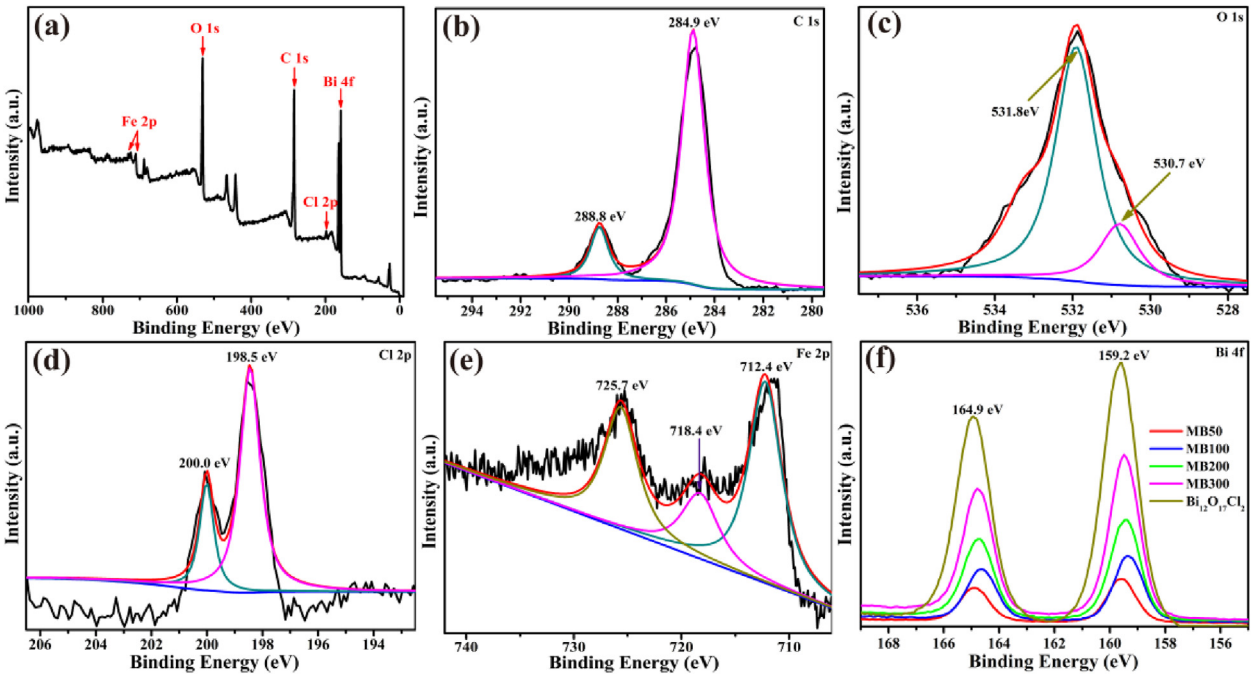

Fig. 4. XPS spectra of BM100: (a) survey, (b) C 1s, (c) O 1s, (d) Cl 2p, (e) Fe 2p and Bi 4f spectra of various MB*x* composites and Bi12O17Cl2.

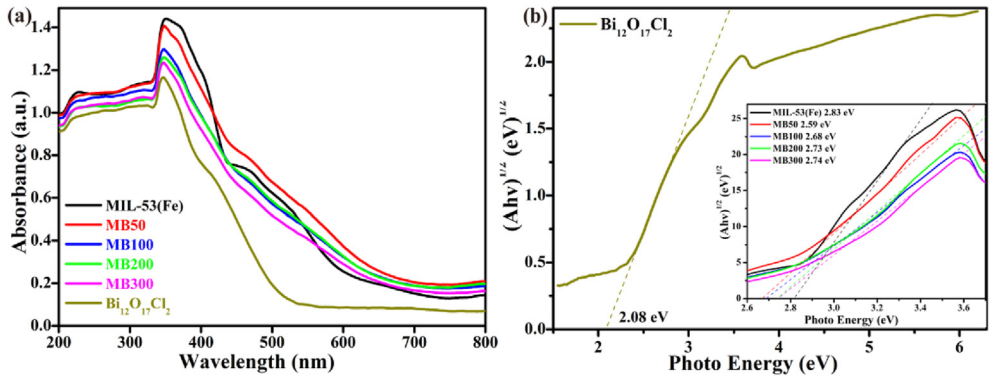

Fig. 5. (a) UV–vis DRS spectra and (b) E_g plots of $Bi_{12}O_{17}Cl_2$, MIL-53(Fe) and MB*x* composites.

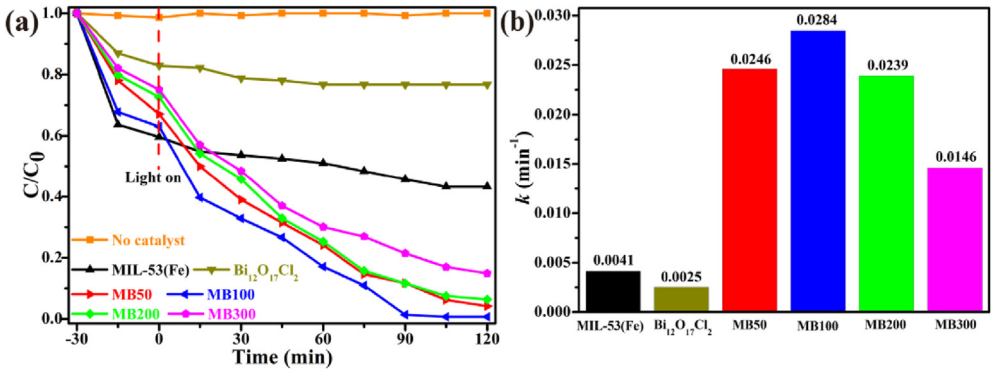

Fig. 6. (a) Cr(VI) photoreduction curves and (b) the corresponding reaction rates over the different photocatalysts. Conditions: dosage = 0.5 g/L, Cr(VI) = 10 mg/L, pH = 2.

the MB100 can be deemed as an remarkable photocatalyst for Cr(VI) reduction.

3.2.1. *Effect of initial pH on Cr(VI) removal*

The initial pH is important in Cr(VI) removal due to it not only connects with the existing species of Cr(VI) ions but also changes the surface electrical properties of the as-prepared photocatalysts [59]. It can be observed that the pH value had a noticeable impact on the adsorption-photocatalytic reaction process (Fig. 7(a)). When the initial pH value was 2.0, 99.2% of Cr(VI) ions were reduced within 120 min under white light irradiation. However, it was obvious that the removal efficiencies of Cr(VI) significantly decreased with the increasing of pH values. When the pH value was 8.0, only 13.3% of Cr(VI) ions were removed. This result should be ascribed to the Cr(VI) ions displayed various forms under different pH conditions [59]. Being compared to the neutral and alkaline solutions, $Cr_2O_7^{2-}$ and $HCrO_4^-$ were the dominating species when pH is less than 6.0 [31], thus the abundant H^+ can enhance the reduction process by photo-generated electrons (Equations (2) and (3)) [58,62]. It was obvious that MB100 exhibited stronger adsorption capacity when pH being 2.0 (36.4%), which was ascribed to the corresponding zeta potential changed from positive to negative with the increasing pH values. Fig. 7(b) showed that the zero potential point of MB100 was 3.79, hence the surface of MB100 was inclined to adsorb Cr(III) cations and to electrostatically repel Cr(VI) anions when pH was greater than 3.79. Moreover, under

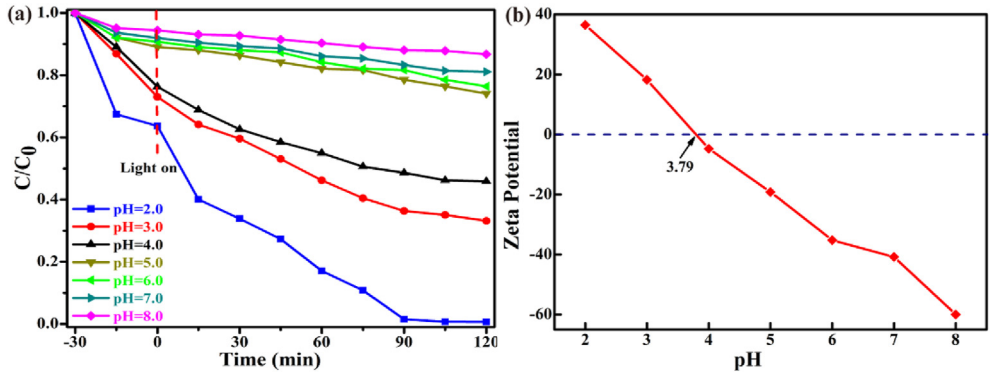

Fig. 7. (a) Effect of different initial pH on the Cr(VI) removal and (b) zeta potential of MB100 under various pH conditions. Conditions: photocatalyst MB100 dosage = 0.5 g/L, Cr(VI) = 10 mg/L.

high-pH conditions, the $Cr(OH)_3$ precipitates could generate on the surface of MB100 (Equation (4)) [31], resulting a sharp decrease in Cr(VI) reduction efficiency.

$$Cr_2O_7^{2-} + 14H^+ + 6e^- \rightarrow 2Cr^{3+} + 7H_2O \quad (2)$$

$$HCrO_4^- + 7H^+ + 3e^- \rightarrow Cr^{3+} + 4H_2O \quad (3)$$

$$CrO_4^{2-} + 4H_2O + 3e^- \rightarrow Cr(OH)_3 + 5OH^- \quad (4)$$

3.2.2. Reusability and stability of BM100

The cyclic experiment of Cr(VI) photoreduction was also performed to explore the reusability and stability of the as-prepared MB100. As depicted in Fig. 8(a), the photocatalytic efficiency of MB100 still maintained at 87.7% after 4 runs of Cr(VI) removal experiments [63]. Furthermore, the PXRD patterns of MB100 after the photocatalytic reaction remained its original crystal structure (Fig. 8(b)), suggesting that the chemical composition of MB100 was not damaged even after four cycles of the photocatalytic processes. Therefore, it can be concluded that MB100 can be deemed as a prominent material for treating Cr(VI)-containing wastewater.

3.3. Possible photocatalytic mechanism

The separation efficiencies of photo-generated carriers of the as-prepared materials were investigated by PL spectra and electrochemical impedance spectra (EIS) [64]. As illustrated in Fig. 9(a), the distinct emission peaks at the excitation wavelength of 620 nm can be clearly observed for all the materials. The $Bi_{12}O_{17}Cl_2$ and MIL-53(Fe) exhibited comparatively strong PL intensity, while the MB*x* composites possessed much lower PL signals. This experimental phenomenon indicated that the construction of composites between $Bi_{12}O_{17}Cl_2$ and MIL-53(Fe) could accelerate migration rates of photo-generated carriers. This speculation can be further assessed by EIS analysis. As shown in Fig. 9(b), the diameters of arc radius followed the order of $Bi_{12}O_{17}Cl_2$ > MIL-53(Fe) > MB300 > MB200 > MB50 > MB100, confirming that MB100 displayed more outstanding charge separation efficiency at heterojunction interface than the other binary composite materials, which was the major factor for determining the apparent photocatalytic reaction rate [65].

To explore the Cr(VI) removal mechanism over the MB100, the valence states of MB100 were explored by Mott-Schottky measurements. Fig. 10 showed the C^{-2} value was positively proportional to the potential, indicating that both MIL-53(Fe) and $Bi_{12}O_{17}Cl_2$ were n-type semiconductors [66–69]. Normally, the conduction band potential (E_{CB}) was more negative 0.1 eV than the flat band potential (E_{FB}) for most of n-type semiconductors [70]. Because the E_{FB} values of MIL-53(Fe) and $Bi_{12}O_{17}Cl_2$ were −0.51 and −0.69 eV *vs* the Ag/AgCl electrode, respectively, so the E_{CB} of $Bi_{12}O_{17}Cl_2$ and lowest unoccupied orbital (LUMO) of MIL-53(Fe) were −0.59 and −0.41eV *vs* NHE. Based on the following calculation formula of $E_g = E_{VB} - E_{CB}$, the valence band potential (E_{VB}) of $Bi_{12}O_{17}Cl_2$ and highest occupied orbital (HOMO) of MIL-53(Fe) were determined as +1.49 and + 2.42 eV, respectively, which were similar to the previous reports [27,38].

Free radical capture tests were also executed to affirm the major active species involved in the photoreduction process. In this study, isopropanol (IPA, 0.2 mmol L^{-1}), ethylenediaminetetra acetic acid disodium (EDTA-2Na, 0.2 mmol L^{-1}), p-benzoquinone (BQ, 0.2 mmol L^{-1}) and silver nitrate ($AgNO_3$, 0.2 mmol L^{-1}) were applied to trap hydroxyl radical (·OH), photo-generated hole (h^+), superoxide radical ($^\bullet O_2^-$) and photo-generated electron (e^-), respectively [71]. As shown in Fig. 11(a), the photoreduction efficiency was significantly inhibited with the presence of $AgNO_3$, suggesting that photo-generated e^- played significant role in Cr(VI) removal [72,73]. Furthermore, The $^\bullet O_2^-$ active species trapping experiment was carried out under a nitrogen ambient to explore its role in the reduction of Cr(VI). As shown in Fig. 11(a), the efficiency of Cr(VI) reduction was promoted in N_2 atmosphere. This phenomenon illustrated that trapping of electrons by O_2 was a competing reaction for Cr(VI) removal [74]. On the other hand, this result indicated that photo-generated electrons played major role in the photoreduction process, which supported the result of using $AgNO_3$ as electron capture agent. Furthermore, it was worth noting that the addition of BQ could suppress the photocatalytic efficiency in this study, revealing that the $^\bullet O_2^-$ was an active radical in reducing Cr(VI) ions. The similar phenomena can be found in the other Cr(VI) photoreduction reaction systems from our previous studies [59,60]. It was interesting that the addition of IPA also caused the decrease of Cr(VI) removal, which should be ascribed to the equilibrium transmitting to Cr(VI) as shown in Equations (5)–(7) [59]. Additionally, the photocatalytic activity was reinforced by introducing EDTA-2Na, which was attributed to the reaction between EDTA-2Na and h^+ could enhance the migration and transfer of photo-generated electrons [31].

$$^\bullet O_2^- + H+ \rightarrow {}^\bullet HO_2 \quad (5)$$

$$^\bullet HO_2 + {}^\bullet O_2^- + H^+ \rightarrow H_2O_2 + O_2 \quad (6)$$

$$H_2O_2 + Cr(III) + H^+ \rightarrow Cr(VI) + H_2O + {}^\bullet HO \quad (7)$$

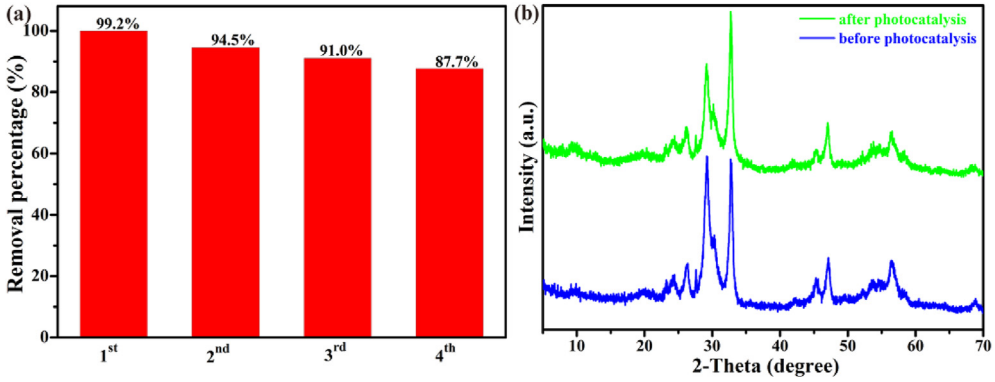

Fig. 8. (a) Recycling experiments for the Cr(VI) reduction over the MB100 and (b) PXRD patterns of MB100 before and after the cyclic experiments.

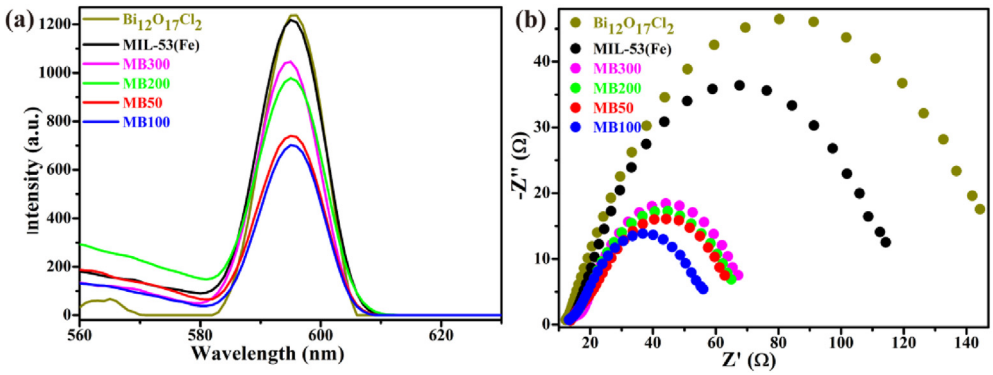

Fig. 9. (a) Photoluminescence spectra and (b) EIS Nyquist impedance plots of $Bi_{12}O_{17}Cl_2$, MIL-53(Fe) and MB*x* composites.

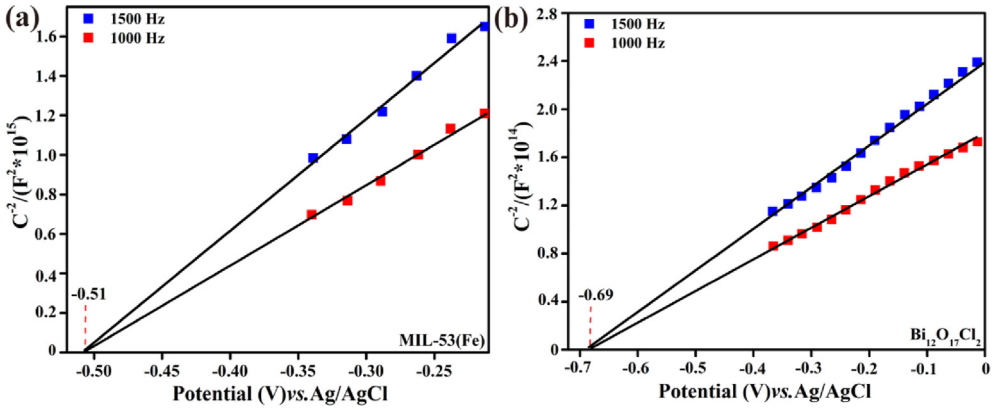

Fig. 10. (a) Mott-Schottky curves of MIL-53(Fe) and (b) $Bi_{12}O_{17}Cl_2$ at different frequencies.

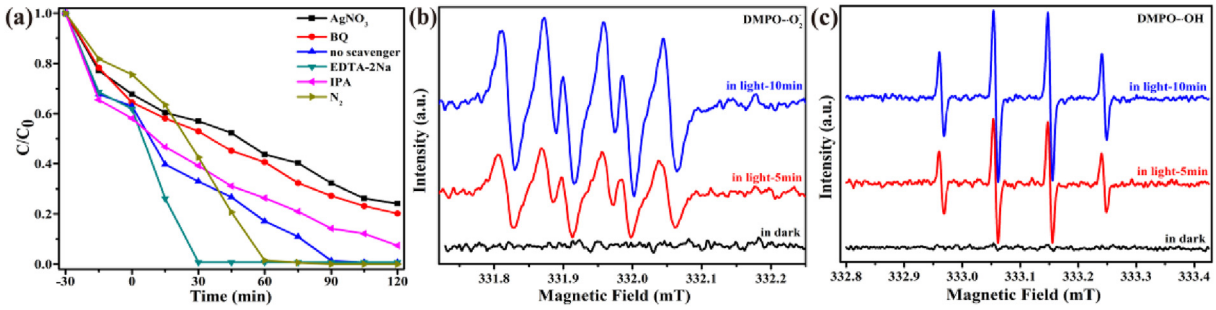

Fig. 11. (a) Reactive species trapping experiments with different scavengers, (b)–(c) ESR spectra of DMPO-$^{\bullet}O_2^-$ and DMPO-··OH adducts generated during the photoreduction process.

Based on the aforementioned results, a Z-scheme photocatalytic mechanism was described in Fig. 12. Firstly, both $Bi_{12}O_{17}Cl_2$ and MIL-53(Fe) were excited by used xenon lamp to generate photo-generated electrons and holes. Then, the produced electrons on the LUMO of MIL-53(Fe) were inclined to couple with holes on the VB of $Bi_{12}O_{17}Cl_2$, enhancing the photo-generated carriers transfer and accumulating more free electrons on the CB of $Bi_{12}O_{17}Cl_2$. Since the E_{CB} of $Bi_{12}O_{17}Cl_2$ was estimated as −0.59 eV *vs* NHE, which was more negative than Cr(VI)/Cr(III) potential (+1.05 eV *vs* NHE) [60]. As a result, Cr(VI) ions could be effectively transformed into Cr(III) on the CB of $Bi_{12}O_{17}Cl_2$。 Meanwhile, the remaining holes on the HOMO of MIL-53(Fe) may react with H_2O to generate ·OH radicals (H_2O/·OH redox potential being 2.40 eV *vs* NHE) [59], which was demonstrated to play only a small role in Cr(III) oxidation. This behavior can kill two birds with one stone, namely further improving the separation of photo-generated charge carriers [71]. Moreover, the Fe_3-μ_3-oxo clusters in MIL-53(Fe) could also trigger the Cr(VI) reduction process, since the linker to metal cluster charge transfer (LCCT) may cause the reduction of Fe(III) to Fe(II), which was beneficial to Cr(VI) removal [14,39].

To verify the above conjecture, ESR technique was applied to further affirm the major reactive species formed during the photoreduction process. As depicted in Fig. 11 (b) and (c), conspicuous signals of DMPO-$^{\bullet}O_2^-$ and DMPO-··OH adducts were detected after the white light illumination for 5 and 10 min, qualitatively confirming the generation of $^{\bullet}O_2^-$ and ·OH radicals in the experimental system. Considering that the E_{VB} of $Bi_{12}O_{17}Cl_2$ was more negative than the H_2O/·OH redox potential [59], so it was not

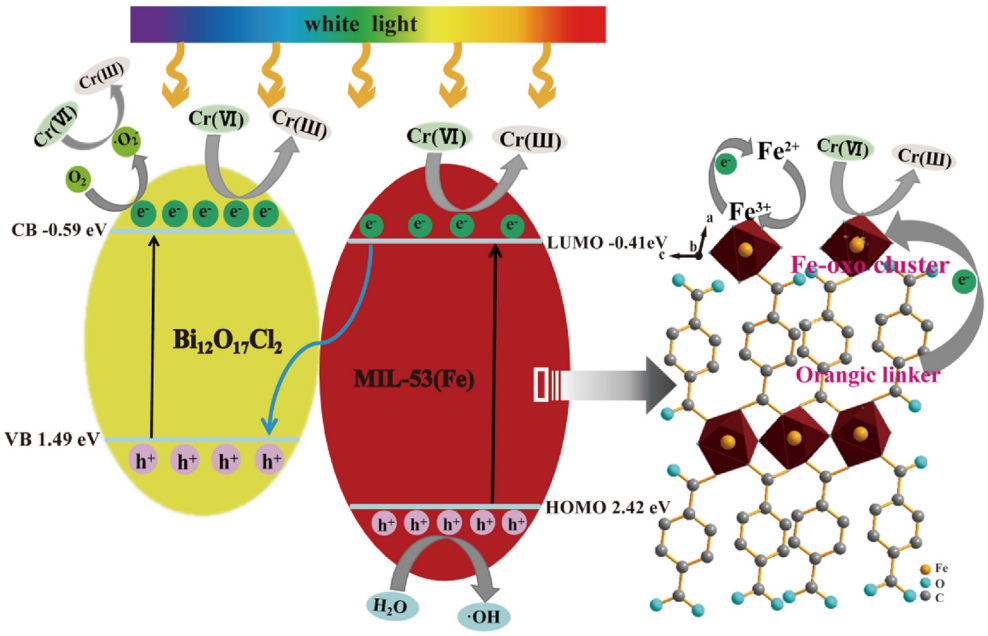

Fig. 12. A schematic diagram of Cr(VI) photoreduction over the MB100 under white light illumination.

thermodynamically allowable for the ·OH production on the VB of $Bi_{12}O_{17}Cl_2$. Therefore, the photocatalytic mechanism in this study was determined to be Z-scheme rather than II-scheme reaction mechanism [75,76].

4. Conclusions

Z-scheme MB*x* composites were easily constructed, which exhibited improved Cr(VI) reduction performances than the MIL-53(Fe) and $Bi_{12}O_{17}Cl_2$ under white light irradiation. Several characterization techniques including PL and electrochemical analysis proved that the formation of composites can facilitate migration and separation of photoinduced charge carriers. Moreover, pH values played significant role in the Cr(VI) removal. Meanwhile, the cycle experiments demonstrated that the MB100 composite possessed good stability and reusability. The findings in this research supply a novel insight into fabrication of bismuth-rich bismuth oxychloride/MOFs hybrids photocatalysts, which might be had great potential for treating Cr-containing wastewater.

CRediT authorship contribution statement

Hua Li: Data curation, Investigation, Visualization, Writing - original draft. **Chen Zhao:** Resources, Investigation, Validation. **Xia Li:** Resources. **Huifen Fu:** Resources. **Zhihua Wang:** Funding acquisition, Supervision, Project administration. **Chong-Chen Wang:** Conceptualization, Funding acquisition, Supervision, Project administration, Writing - review & editing.

Declaration of competing interest

On behalf of all authors, I declare that we do not have any commercial or associative interest that represents a conflict of interest in connection with the work entitled "Boosted photocatalytic Cr(VI) reduction over Z-scheme MIL-53(Fe)/$Bi_{12}O_{17}Cl_2$ composites under white light".

Acknowledgement

This work was supported by the National Natural Science Foundation of China (21876008) and Beijing Natural Science Foundation (No. 8202016) and Beijing Talent Project (No. 2019A22).

Appendix A. Supplementary data

Supplementary data to this article can be found online at https://doi.org/10.1016/j.jallcom.2020.156147.

References

[1] H. Lü, Y.-H. Huang, X.-J. Huang, Q.-Y. Cai, The state of particulate matter contamination, particulate matter-bound heavy metals, and persistent organic pollutants (POPs) in megacities, China, Curr. Opin. Environ. Sci. health 8 (2016) 15–22, https://doi.org/10.1016/j.coesh.2019.01.001.
[2] M. Venier, R.A. Hites, Time trend analysis of atmospheric POPs concentrations in the great lakes region since 1990, Environ. Sci. Technol. 44 (2010) 8050–8055, https://doi.org/10.1021/es101656u.
[3] Y. Zhao, L. Yang, Q. Wang, Modeling persistent organic pollutant (POP) partitioning between tree bark and air and its application to spatial monitoring of atmospheric POPs in Mainland China, Environ. Sci. Technol. 42 (2008) 6046–6051, https://doi.org/10.1021/es800188q.
[4] M.F. Meyer, S.M. Powers, S.E. Hampton, An evidence synthesis of pharmaceuticals and personal care products (PPCPs) in the environment: imbalances among compounds, Sewage Treatment Techniques, and Ecosystem Types, Environ. Sci. Technol. 53 (2019) 12961–12973, https://doi.org/10.1021/acs.est.9b02966.
[5] Enric Brillas, C.A. Martínez-Huitle, Photocatalytic decontamination of wastewater containing organic dyes by metal-organic frameworks and their derivatives, Appl. Catal. B Environ. 166–167 (2015) 603–643, https://doi.org/10.1002/cctc.201600808.
[6] M. Owlad, M.K. Aroua, W.A.W. Daud, S. Baroutian, Removal of hexavalent chromium-contaminated water and wastewater: a review, Water, Air, Soil Pollut. 200 (2009) 59–77, https://doi.org/10.1007/s11270-008-9893-7.
[7] T.L. DesMarias, M. Costa, Mechanisms of chromium-induced toxicity, Curr. Opin. in Toxicol. 14 (2019) 1–7, https://doi.org/10.1016/j.cotox.2019.05.003.
[8] Z. Shao, C. Huang, Q. Wu, Y. Zhao, W. Xu, Y. Liu, J. Dang, H. Hou, Ion exchange collaborating coordination substitution: more efficient Cr(VI) removal performance of a water-stable Cu^{II}-MOF material, J. Hazard Mater. 378 (2019) 120719–120727, https://doi.org/10.1016/j.jhazmat.2019.05.112.
[9] C.A. Kozlowskia, W. Walkowiak, Removal of chromium(VI) from aqueous solutions by polymer inclusion membranes, Water Res. 36 (2002) 4870–4876, https://doi.org/10.1016/s0043-1354(02)00216-6.
[10] S. Sriram, I.M. Nambi, R. Chetty, Hexavalent chromium reduction through

redox electrolytic cell with urea and cow urine as anolyte, J. Environ. Manag. 232 (2019) 554–563, https://doi.org/10.1016/j.jenvman.2018.11.071.
[11] Z. Wan, D.-W. Cho, C.W. Tsang, M. Li, T. Sun, F. Verpoort, Concurrent adsorption and micro-electrolysis of Cr(VI) by nanoscale zerovalent iron/biochar/Ca-alginate, composite Environ. Pollut. 247 (2019) 410–420, https://doi.org/10.1016/j.envpol.2019.01.047.
[12] L. Shen, L. Huang, S. Liang, R. Liang, N. Qin, L. Wu, Electrostatically derived self-assembly of NH_2-mediated zirconium MOFs with graphene for photocatalytic reduction of Cr(VI), RSC Adv. 4 (2014) 2546–2549, https://doi.org/10.1039/C3RA45848B.
[13] A. Rauf, Md S.A. S. Shah, G.H. Choi, U.B. Humayoun, D.H. Yoon, J.W. Bae, J. Park, Woo-Jae Kim, P.J. Yoo, Facile synthesis of hierarchically structured Bi_2S_3/Bi_2WO_6 photocatalysts for highly efficient reduction of Cr(VI), ACS Sustain. Chem. Eng. 3 (2015) 2847–2855, https://doi.org/10.1021/acssuschemeng.5b00783.
[14] L. Shi, T. Wang, H. Zhang, K. Chang, X. Meng, H. Liu, J. Ye, An amine-functionalized iron(III) Metal-Organic Framework as efficient visible-light photocatalyst for Cr(VI) reduction, Advanced Sci 2 (2015) 1500006–1500014, https://doi.org/10.1002/advs.201500006.
[15] R. Yuan, C. Yue, J. Qiu, F. Liu, A. Li, Highly efficient sunlight-driven reduction of Cr(VI) by TiO_2@NH_2-MIL-88B(Fe) heterostructures under neutral conditions, Appl. Catal. B Environ. 251 (2019) 229–239, https://doi.org/10.1016/j.apcatb.2019.03.068.
[16] J. Jiang, K. Zhao, X. Xiao, L. Zhang, Synthesis and facet-dependent photoreactivity of BiOCl single-crystalline nanosheets, J. Am. Chem. Soc. 134 (2012) 4473–4476, https://doi.org/10.1021/ja210484t.
[17] K.-L. Zhang, C.-M. Liu, F.-Q. Huang, C. Zheng, W.-D. Wang, Study of the electronic structure and photocatalytic activity of the BiOCl photocatalyst, Appl. Catal. B Environ. 68 (2006) 125–129, https://doi.org/10.1016/j.apcatb.2006.08.002.
[18] S. Weng, B. Chen, L. Xie, Z. Zheng, P. Liu, Facile in situ synthesis of a Bi/BiOCl nanocomposite with high photocatalytic activity, J. Mater. Chem. 1 (2013) 3068, https://doi.org/10.1039/C2TA01004F.
[19] J. Cao, B. Xu, B. Luo, H. Lin, S. Chen, Novel BiOI/BiOBr heterojunction photocatalysts with enhanced visible light photocatalytic properties, Catal. Commun. 13 (2011) 63–68, https://doi.org/10.1016/j.catcom.2011.06.019.
[20] T.B. Li, G. Chen, C. Zhou, Z.Y. Shen, R.C. Jin, J.X. Sun, New photocatalyst BiOCl/BiOI composites with highly enhanced visible light photocatalytic performances, Dalton Trans. 40 (2011) 6751–6758, https://doi.org/10.1039/c1dt10471c.
[21] Y. Gao, S. Li, Y. Li, L. Yao, H. Zhang, Accelerated photocatalytic degradation of organic pollutant over metal-organic framework MIL-53(Fe) under visible LED light mediated by persulfate, Appl. Catal. B Environ. 202 (2017) 165–174, https://doi.org/10.1016/j.apcatb.2016.09.005.
[22] G. He, C. Xing, X. Xiao, R. Hu, X. Zuo, J. Nan, Facile synthesis of flower-like $Bi_{12}O_{17}Cl_2$/β-Bi_2O_3 composites with enhanced visible light photocatalytic performance for the degradation of 4-tert-butylphenol, Appl. Catal. B Environ. 170–171 (2015) 1–9, https://doi.org/10.1016/j.apcatb.2015.01.015.
[23] C. Zhou, C. Lai, P. Xu, G. Zeng, D. Huang, C. Zhang, M. Cheng, L. Hu, J. Wan, Y. Liu, W. Xiong, Y. Deng, M. Wen, In situ grown AgI/$Bi_{12}O_{17}Cl_2$ heterojunction photocatalysts for visible light degradation of sulfamethazine: efficiency, pathway and mechanism, ACS Sustain. Chem. Eng. 6 (2018) 4174–4184, https://doi.org/10.1021/acssuschemeng.7b04584.
[24] C. Zhou, C. Lai, P. Xu, G. Zeng, D. Huang, Z. Li, C. Zhang, M. Cheng, L. Hu, J. Wan, F. Chen, W. Xiong, R. Deng, Rational design of carbon-doped carbon nitride/$Bi_{12}O_{17}Cl_2$ composites: a promising candidate photocatalyst for boosting visible-light-driven photocatalytic degradation of tetracycline, ACS Sustain. Chem. Eng. 6 (2018) 6941–6949, https://doi.org/10.1021/acssuschemeng.8b00782.
[25] C. Bi, J. Cao, H. Lin, Y. Wang, S. Chen, BiOI/$Bi_{12}O_{17}Cl_2$: a novel heterojunction composite with outstanding photocatalytic and photoelectric performances, Appl. Catal. B Environ. 166 (2016) 267–270, https://doi.org/10.1016/j.matlet.2015.12.089.
[26] Y. Peng, P.-P. Yu, Q.-G. Chen, H.-Y. Zhou, A.-W. Xu, Facile fabrication of $Bi_{12}O_{17}Br_2$/$Bi_{24}O_{31}Br_{10}$ type II heterostructures with high visible photocatalytic activity, J. Phys. Chem. C 119 (2015) 13032–13040, https://doi.org/10.1021/acs.jpcc.5b02132.
[27] C.-Y. Wang, X. Zhang, H.-B. Qiu, W.-K. Wang, G.-X. Huang, J. Jiang, H.-Q. Yu, Photocatalytic degradation of bisphenol A by oxygen-rich and highly visible-light responsive $Bi_{12}O_{17}Cl_2$ nanobelts, Appl. Catal. B Environ. 200 (2016) 659–665, https://doi.org/10.1016/j.apcatb.2016.07.054.
[28] H. Fu, X.-X. Song, L. Wu, C. Zhao, P. Wang, C.-C. Wang, Room-temperature preparation of MIL-88A as a visible-light-driven photocatalyst for degradation of rhodamine B and bisphenol A, Mater. Res. Bull. 125 (2020) 110806–110814, https://doi.org/10.1016/j.materresbull.2020.110806.
[29] Y.-C. Zhou, P. Wang, H. Fu, C. Zhao, C.-C. Wang, Ternary Ag/Ag_3PO_4/MIL-125-NH_2 Z-scheme heterojunction for boosted photocatalytic Cr(VI) cleanup under visible light, Chin. Chem. Lett. (2020), https://doi.org/10.1016/j.cclet.2020.02.048.
[30] P. Li, M. Guo, Q. Wang, Z. Li, C. Wang, N. Chen, C.-C. Wang, C. Wan, S. Chen, Controllable synthesis of cerium zirconium oxide nanocomposites and their application for photocatalytic degradation of sulfonamides, Appl. Catal. B Environ. 259 (2019) 118107–118118, https://doi.org/10.1016/j.apcatb.2019.118107.
[31] X.-H. Yi, F.-X. Wang, X.-D. Du, P. Wang, C.-C. Wang, Facile fabrication of BUC-21/g-C_3N_4 composites and their enhanced photocatalytic Cr(VI) reduction performances under simulated sunlight, Appl. Organomet. Chem. 33 (2019) 4621–4632, https://doi.org/10.1002/aoc.4621.
[32] D. Saha, Z. Bao, F. Jia, S. Deng, Adsorption of CO_2, CH_4, N_2O, and N_2 on MOF-5, MOF-177, and zeolite 5A, Environ. Sci. Technol. 44 (2010) 1820–1826, https://doi.org/10.1021/es9032309.
[33] Y. Zhang, Z. Jin, Boosting photocatalytic hydrogen evolution achieved by NiSx coupled with g-C_3N_4@ZIF-67 heterojunction, J. Phys. Chem. C 123 (2019) 18248–18263, https://doi.org/10.1021/acs.jpcc.9b04695.
[34] J. Guo, J.-J. Li, C.-C. Wang, Adsorptive removal of Cr(VI) from simulated wastewater in MOF BUC-17 ultrafine powder, J. Environ. Chem. Eng. 7 (2019) 102909–102917, https://doi.org/10.1016/j.jece.2019.102909.
[35] H. Bux, C. Chmelik, R. Krishna, J. Caro, Ethene/ethane separation by the MOF membrane ZIF-8: molecular correlation of permeation, adsorption, diffusion, J. Membr. Sci. 369 (2011) 284–289, https://doi.org/10.1016/j.memsci.2010.12.001.
[36] H. Fu, Z. Wang, X. Wang, P. Wang, C.-C. Wang, Formation mechanism of rod-like ZIF-L and fast phase transformation from ZIF-L to ZIF-8 with morphology changes controlled by polyvinylpyrrolidone and ethanol, CrystEngComm 20 (2018) 1473–1477, https://doi.org/10.1039/c7ce02073b.
[37] T. Loiseau, C. Serre, C. Huguenard, G. Fink, F. Taulelle, M. Henry, T. Bataille, G. Férey, A rationale for the large breathing of the porous aluminum terephthalate (MIL-53) upon hydration, Chemistry 10 (2004) 1373–1382, https://doi.org/10.1002/chem.200305413.
[38] L. Tang, Z. Lv, Y. Xue, L. Xu, W. Qiu, C. Zheng, W. Chen, M. Wu, MIL-53(Fe) incorporated in the lamellar BiOBr: promoting the visible-light catalytic capability on the degradation of rhodamine B and carbamazepine, Chem. Eng. J. 374 (2019) 975–982, https://doi.org/10.1016/j.cej.2019.06.019.
[39] W. Huang, N. Liu, X. Zhang, M. Wu, L. Tang, Metal organic framework g-C_3N_4/MIL-53(Fe) heterojunctions with enhanced photocatalytic activity for Cr(VI) reduction under visible light, Appl. Surf. Sci. 425 (2017) 107–116, https://doi.org/10.1016/j.apsusc.2017.07.050.
[40] L. Hu, G. Deng, W. Lu, S. Pang, X. Hu, Deposition of CdS nanoparticles on MIL-53(Fe) metal-organic framework with enhanced photocatalytic degradation of RhB under visible light irradiation, Appl. Surf. Sci. 410 (2017) 401–413, https://doi.org/10.1016/j.apsusc.2017.03.140.
[41] M. Xu, J. Yang, L. Liu, Y. Cui, B. Liang, Performance enhancement strategies of bi-based photocatalysts: a review on recent progress, Chem. Eng. J. 389 (2020) 124402–124468, https://doi.org/10.1016/j.cej.2020.124402.
[42] Z. Yang, X. Xu, X. Liang, C. Lei, Y. Wei, P. He, B. Lv, H. Ma, Z. Lei, MIL-53(Fe)-graphene nanocomposites: efficient visible-light photocatalysts for the selective oxidation of alcohols, Appl. Catal. B Environ. 198 (2016) 112–123, https://doi.org/10.1016/j.apcatb.2016.05.041.
[43] Q. Hu, J. Di, B. Wang, M. Ji, Y. Chen, J. Xia, H. Li, Y. Zhao, In-situ preparation of NH_2-MIL-125(Ti)/BiOCl composite with accelerating charge carriers for boosting visible light photocatalytic activity, Appl. Surf. Sci. 466 (2019) 525–534, https://doi.org/10.1016/j.apsusc.2018.10.020.
[44] S.R. Zhu, P.F. Liu, M.K. Wu, W.N. Zhao, G.C. Li, K. Tao, F.Y. Yi, L. Han, Enhanced photocatalytic performance of BiOBr/NH_2-MIL-125(Ti) composite for dye degradation under visible light, Dalton Trans. 45 (2016) 17521–17529, https://doi.org/10.1039/C6DT02912D.
[45] F. Millange, C. Serre, G. Férey, Synthesis, structure determination and properties of MIL-53as and MIL-53ht: the first CrIII hybrid inorganic–organic microporous solids: CrIII(OH)·{O_2C-C_6H_4-CO_2·{HO_2C-C_6H_4-CO_2H}$_x$, Chem. Commun. 8 (2002) 822–823, https://doi.org/10.1039/B201381A.
[46] P. Horcajada, C. Serre, G. Maurin, N.A. Ramsahye, F. Balas, M. Vallet-Regí, M. l Sebban, F. Taulelle, G. Férey, Flexible porous Metal-Organic Frameworks for a controlled drug delivery, J. Am. Chem. Soc. 130 (2008) 6774–6780, https://doi.org/10.1021/ja710973k.
[47] A. Banerjee, R. Gokhale, S. Bhatnagar, J. Jog, M. Bhardwaj, B. Lefez, B. Hannoyer, S. Ogale, MOF derived porous carbon–Fe_3O_4 nanocomposite as a high performance, recyclable environmental super adsorbent, J. Mater. Chem. 22 (2012) 19694–19700, https://doi.org/10.1039/c2jm33798c.
[48] C. Gong, D. Chen, X. Jiao, Q. Wang, Continuous hollow α-Fe_2O_3 and α-Fe fibers prepared by the sol–gel method, Mater. Chem. 12 (2002) 1844–1847, https://doi.org/10.1039/b201243j.
[49] R. Tanwar, S. Kumar, U.K. Mandal, Photocatalytic activity of PANI/Fe0 doped BiOCl under visible light-degradation of Congo red dye, Photochem. Photobiol.: Inside Chem. 333 (2017) 105–116, https://doi.org/10.1016/j.jphotochem.2016.10.022.
[50] B. Lin, C. Xue, X. Yan, G. Yang, G. Yang, B. Yang, Facile fabrication of novel SiO_2/g-C_3N_4 core–shell nanosphere photocatalysts with enhanced visible light activity, Appl. Surf. Sci. 357 (2015) 346–355, https://doi.org/10.1016/j.apsusc.2015.09.041.
[51] S.K. Tam, J. Dusseault, S. Polizu, M. Ménard, J.-P. Hallé, L'H. Yahia, Physicochemical model of alginate-poly-L-lysine microcapsules defined at the micrometric/nanometric scale using ATR-FTIR, XPS, and ToF-SIMS, Biomaterials 26 (2005) 6950–6961, https://doi.org/10.1016/j.biomaterials.2005.05.007.
[52] C.-Y. Wang, Y.-J. Zhang, W.-K. Wang, D.-N. Pei, G.-X. Huang, J.-J. Chen, X. Zhang, H.-Q. Yu, Enhanced photocatalytic degradation of bisphenol A by Co-doped BiOCl nanosheets under visible light irradiation, Appl. Catal. B Environ. 221 (2018) 320–328, https://doi.org/10.1016/j.apcatb.2017.09.036.
[53] M. Gao, D. Zhang, X. Pu, H. Li, W. Li, X. Shao, D. Lv, B. Zhang, J. Dou, Combustion synthesis of Fe-doped BiOCl with high visible-light photocatalytic activities,

Separ. Purif. Technol. 162 (2016) 114–119, https://doi.org/10.1016/j.seppur.2016.02.024.
[54] R. Li, Z. Chen, M. Cai, J. Huang, P. Chen, G. Liu, W. Lv, Improvement of sulfamethazine photodegradation by Fe(III) assisted MIL-53(Fe)/percarbonate system, Appl. Surf. Sci. 457 (2018) 726–734, https://doi.org/10.1016/j.apsusc.2018.06.294.
[55] W.-M. Zhang, X.-L. Wu, J.-S. Hu, Y.-G. Guo, L.-J. Wan, Carbon coated Fe_3O_4 nanospindles as a superior anode material for lithium on batteries, Adv. Funct. Mater. 18 (2010) 3941–3946, https://doi.org/10.1002/adfm.200801386.
[56] R. Panda, S. Rahuta, J.K. Basu, Preparation of α-Fe_2O_3/MIL-53(Fe) composite by partial thermal decomposition of MIL-53(Fe) nanorods and their photocatalytic activity, RSC Adv. 6 (2016) 80981–80985, https://doi.org/10.1039/C6RA15792K.
[57] Y. Yu, C. Cao, H. Liu, P. Li, F. Wei, Y. Jiang, W. Song, A Bi/BiOCl heterojunction photocatalyst with enhanced electron-hole separation and excellent visible light photodegrading activity, Mater. Chem. A. 2 (2014) 1677–1681, https://doi.org/10.1039/c3ta14494a.
[58] X.-Y. Xu, C. Chu, H. Fu, X.-D. Du, P. Wang, W. Zheng, C.-C. Wang, Light-responsive UiO-66-NH_2/Ag_3PO_4 MOF-nanoparticle composites for the capture and release of sulfamethoxazole, Chem. Eng. J. 350 (2018) 436–444, https://doi.org/10.1016/j.cej.2018.06.005.
[59] C. Zhao, Z. Wang, X. Li, X. Yi, H. Chu, X. Chen, C.-C. Wang, Facile fabrication of BUC-21/$Bi_{24}O_{31}Br_{10}$ composites for enhanced photocatalytic Cr(VI) reduction under simulated sunlight, Chem. Eng. J. 389 (2020) 123431–123444, https://doi.org/10.1016/j.cej.2019.123431.
[60] X.-H. Yi, S.-Q. Ma, X.-D. Du, C. Zhao, H. Fu, P. Wang, C.-C. Wang, The facile fabrication of 2D/3D Z-scheme g-C_3N_4/UiO-66 heterojunction with enhanced photocatalytic Cr(VI) reduction performance under white light, Chem. Eng. J. 375 (2019) 121944–121957, https://doi.org/10.1016/j.cej.2019.121944.
[61] X. Zhang, Z. Ai, F. Jia, L. Zhang, Generalized one-pot synthesis, characterization, and photocatalytic activity of hierarchical BiOX (X=Cl, Br, I) nanoplate microspheres, J. Phys. Chem. C 112 (2008) 747–753, https://doi.org/10.1021/jp077471t.
[62] X. Xiao, R. Hao, M. Liang, X. Zuo, J. Nan, L. Li, W. Zhang, One-pot solvothermal synthesis of three-dimensional(3D) BiOI/BiOCl composites with enhanced visible-light photocatalytic activities for the degradation of bisphenol-A, J. Hazard Mater. 233–234 (2012) 122–130, https://doi.org/10.1016/j.jhazmat.2012.06.062.
[63] K.-L. Zhang, C.-M. Liu, F.-Q. Huang, C. Zheng, W.-D. Wang, Study of the electronic structure and photocatalytic activity of the BiOCl photocatalyst, Appl. Catal. B Environ. 68 (2006) 125–129, https://doi.org/10.1016/j.apcatb.2006.08.002.
[64] L. Zhang, C.-G. Niu, C. Liang, X.-J. Wen, D.-W. Huang, H. Guo, X.-F. Zhao, G.-M. Zeng, One-step in situ synthesis of CdS/SnO_2 heterostructure with excellent photocatalytic performance for Cr(VI) reduction and tetracycline degradation, Chem. Eng. J. 352 (2018) 863–875, https://doi.org/10.1016/j.cej.2018.07.102.
[65] Y.-C. Nie, F. Yu, L.-C. Wang, Q.-J. Xing, X. Liu, Y. Pei, J.-P. Zou, W.-L. Dai, Y. Li, S.L. Sui, Photocatalytic degradation of organic pollutants coupled with simultaneous photocatalytic H_2 evolution over graphene quantum dots/Mn-N-TiO_2/g-C_3N_4 composite catalysts: performance and mechanism, Appl. Catal. B Environ. 227 (2018) 312–321, https://doi.org/10.1016/j.apcatb.2018.01.033.
[66] W. Guo, J. Zhang, G. Li, C. Xu, Enhanced photocatalytic activity of P-type (K, Fe) co-doped g-C_3N_4 synthesized in self-generated NH_3 atmosphere, Appl. Surf. Sci. 470 (2019) 99–106, https://doi.org/10.1016/j.apsusc.2018.10.234.
[67] L. Shen, R. Liang, M. Luo, F. Jing, L. Wu, Electronic effects of ligand substitution on metal-organic framework photocatalysts: the case study of UiO-66, Phys. Chem. Chem. Phys. 17 (2015) 117–121, https://doi.org/10.1039/c4cp04162c.
[68] L.-P. Sun, S.-Y. Niu, J. Jin, G.-D. Yang, L. Ye, Crystal structure and surface photovoltage of a series of Ni(II) coordination supramolecular polymer, Inorg. Chem. Commun. 9 (2006) 679–682, https://doi.org/10.1016/j.inoche.2006.03.027.
[69] Y.-C. Zhou, X.-Y. Xu, P. Wang, H. Fu, C. Zhao, C.-C. Wang, Facile fabrication and enhanced photocatalytic performance of visible light responsive UiO-66-NH_2/Ag_2CO_3 composite, Chin. J. Catal. 40 (2019) 1912–1923, https://doi.org/10.1016/S1872-2067(19)63433-9.
[70] C. Zhao, Z. Wang, X. Chen, H. Chu, H. Fu, C.-C. Wang, Robust photocatalytic benzene degradation using mesoporous disk-like N-TiO_2 derived from MIL-125(Ti), Chin. J. Catal. 41 (2020) 1186–1197, https://doi.org/10.1016/S1872-2067(19)63516-3.
[71] X. Hu, W. Wang, G. Xie, H. Wang, X. Tan, Q. Jin, D. Zhou, Y. Zhao, Ternary assembly of g-C_3N_4/graphene oxide sheets/$BiFeO_3$ heterojunction with enhanced photoreduction of Cr(VI) under visible-light irradiation, Chemosphere 216 (2019) 733–741, https://doi.org/10.1016/j.chemosphere.2018.10.181.
[72] X. Hu, H. Ji, F. Chang, Y. Luo, Simultaneous photocatalytic Cr(VI) reduction and 2,4,6-TCP oxidation over g-C_3N_4 under visible light irradiation, Catal. Today 224 (2014) 34–40, https://doi.org/10.1016/j.cattod.2013.11.038.
[73] A. Kumar, P. Raizada, P. Singh, R. V Saini, A. K Saini, A. Hosseini-Bandegharaei, Perspective and status of polymeric graphitic carbon nitride based Z-scheme photocatalytic systems for sustainable photocatalytic water purification, Chem. Eng. J. 14 (2019), 123496, https://doi.org/10.1016/j.cej.2019.123496.
[74] W. Yan, Q. Chen, X. Meng, B. Wang, Multicycle photocatalytic reduction of Cr(VI) over transparent PVA/TiO2 nanocomposite films under visible light, Sci. China Mater. 60 (2017) 449–460, https://doi.org/10.1007/s40843-017-9024-9.
[75] N. Tian, H. Huang, Y. He, Y. Guo, T. Zhang, Y. Zhang, Mediator-free direct Z-scheme photocatalytic system: $BiVO_4$/g-C_3N_4 organic-inorganic hybrid photocatalyst with highly efficient visible-light-induced photocatalytic activity, Dalton Trans. 44 (2015) 4297–4307, https://doi.org/10.1039/C4DT03905J.
[76] L. Zhu, H. Li, P. Xia, Z. Liu, D. Xiong, Hierarchical ZnO decorated with CeO_2 nanoparticles as direct Z-Scheme heterojunction for enhanced photocatalytic activity, ACS Appl. Mater. Interfaces 10 (2018) 39679–39687, https://doi.org/10.1021/acsami.8b13782.